

## Article

# Optimization of Composite Cavitation Nozzle Parameters Based on the Response Surface Methodology

Gao Huang<sup>1</sup>, Chengjun Qiu<sup>1,2,3,\*</sup>, Mengtian Song<sup>1,2,\*</sup>, Wei Qu<sup>2,4</sup>, Yuan Zhuang<sup>1</sup>, Kaixuan Chen<sup>1</sup>, Kaijie Huang<sup>1</sup>, Jiaqi Gao<sup>1</sup>, Jianfeng Hao<sup>1</sup> and Huili Hao<sup>1</sup>

<sup>1</sup> College of Mechanical, Naval Architecture & Ocean Engineering, Beibu Gulf University, Qinzhou 535011, China; huanggao2024@163.com (G.H.); zhuangyuan@bbgu.edu.cn (Y.Z.); chenx@bbgu.edu.cn (K.C.); hkjhha@163.com (K.H.); znkjgl@sina.com (J.G.); 18435407763@163.com (J.H.); haohuili0022@163.com (H.H.)

<sup>2</sup> Eastern Michigan Joint College of Engineering, Beibu Gulf University, Qinzhou 535011, China; quwei@bbgu.edu.cn

<sup>3</sup> Guangxi Key Laboratory of Ocean Engineering Equipment and Technology, Qinzhou 535011, China

<sup>4</sup> College of Electronics and Information Engineering, Beibu Gulf University, Qinzhou 535011, China

\* Correspondence: qiuchengjun@bbgu.edu.cn (C.Q.); songmengtian@bbgu.edu.cn (M.S.); Tel.: +86-1817770651 (C.Q.); +86-18377181848 (M.S.)

**Abstract:** Cavitation is typically observed when high-pressure submerged water jets are used. A composite nozzle, based on an organ pipe, can increase shear stress on the incoming flow, significantly enhancing cavitation performance by stacking Helmholtz cavities in series. In the present work, the flow field of the composite nozzle was numerically simulated using Large Eddy Simulation and was paired with the response surface method for global optimizing the crucial parameters of the composite nozzle to examine their effect on cavitation behavior. Utilizing peak gas-phase volume percent as the dependent variable and the runner diameter, Helmholtz chamber diameter, and Helmholtz chamber length as independent variables, a mathematical model was constructed to determine the ideal parameters of the composite nozzle through response surface methodology. The optimized nozzle prediction had an error of only 2.04% compared to the simulation results, confirming the accuracy of the model. To learn more about the cavitation cloud properties, an experimental setup for high-pressure cavitation jets was also constructed. Impact force measurements and high-speed photography tests were among the experiments conducted. The simulated evolution period of cavitation cloud characteristics is highly consistent with the experimental period. In the impact force measurement experiment, the simulated impact force oscillates between 256 and 297 N, and the measured impact force oscillates between 260 N and 289 N, with an error between 1.5% and 2.7%. The simulation model was verified by experimental results. This study provides new insights for the development of cavitation jet nozzle design theory.

**Keywords:** composite submerged nozzle; large eddy simulation; response surface methodology; high-speed photography



**Citation:** Huang, G.; Qiu, C.; Song, M.; Qu, W.; Zhuang, Y.; Chen, K.; Huang, K.; Gao, J.; Hao, J.; Hao, H. Optimization of Composite Cavitation Nozzle Parameters Based on the Response Surface Methodology. *Water* **2024**, *16*, 850. <https://doi.org/10.3390/w16060850>

Academic Editors: Shiqiang Wu and Ang Gao

Received: 16 February 2024

Revised: 8 March 2024

Accepted: 11 March 2024

Published: 15 March 2024



**Copyright:** © 2024 by the authors. Licensee MDPI, Basel, Switzerland. This article is an open access article distributed under the terms and conditions of the Creative Commons Attribution (CC BY) license (<https://creativecommons.org/licenses/by/4.0/>).

## 1. Introduction

Cavitation refers to the process in a fluid flow where, due to changes in the pipeline structure or external conditions, the local fluid pressure drops below the current fluid's saturation vapor pressure. This drop causes tiny bubbles within the fluid to rapidly expand and collapse in a short period, releasing a large amount of energy. Johnson et al. [1] proposed to apply cavitation to water jet technology to improve the jet erosion effect. Relevant studies have shown that under the same conditions of pump pressure and flow rate conditions, the impact pressure of a cavitation jet is 8.6 to 124 times higher than that of a continuous jet [2–4]. Cavitation jet technology has wide applications in fields such as oil extraction, cleaning and rust removal, and metal surface strengthening [5–7].

The cavitation jet nozzle is the core component for generating cavitation and can have a significant impact on the cavitation effect [8–10]. The working conditions inside the cavitation jet nozzle are complex, involving phase transition, high pressure, and high speed. Therefore, the study of the internal phenomenon of the cavitation nozzle mainly relies on numerical simulation [11,12]. Chen et al. [13] confirmed through numerical simulations that cavitation jet corrosion of steel is primarily due to the generation of high-strength shock waves and instantaneous high temperatures when cavitation bubbles collapse. Dong et al. [14] modified the cavity wall contour of the Helmholtz nozzle into a circular arc shape, resulting in a 16.9% increase in turbulent flow energy. Yang et al. [15] captured the growth, shedding, and collapse of cavitation in three nozzle jets using high-speed photography, finding good agreement between experimental images and predicted model images. Dong [16] designed a diagonal nozzle with the  $k-\varepsilon$  model and researched the impact of intake constriction, parallel mid-section. Wang [17] used the proper orthogonal decomposition method (POD) to analyze cavitation cloud characteristics in organ pipe nozzles. Stanley et al. [18] used direct numerical simulation (DNS) to study the creation of a free jet flow and the non-constant flow properties of a free-jet-flow shear layer. The Reynolds-Averaged Navier–Stokes (RANS) method is commonly used for its lower computational demand, but it struggles to describe vortex dynamics and only simulates time-averaged flow characteristics, neglecting transient values in cavitating flow fields [19].

Large Eddy Simulation (LES) can decompose turbulent instantaneous motion into large- and small-scale vortices, which are calculated separately. Large-scale motion needs to be directly calculated through a numerical solution of the motion differential equation. The impact of small-scale motion on large-scale motion will be manifested in a stress term similar to Reynolds stress in the motion equation, which is called sub-grid Reynolds stress. They will be simulated by establishing a model that is a perfect combination of the direct simulation method and the Reynolds-averaged simulation method. With sufficient computational resources, more information on turbulence can be obtained. The method has been extensively used to study nozzle cavitation [20–23]. Kim et al. [24] used LES to investigate the influences of initial momentum thickness on free jet flow in a circular hole, discovering that these factors have a significant impact on the free jet's flow characteristics. Fang [25] compared LES results with experiments to better understand organ pipe nozzles. Li et al. [26] used LES to study the flow characteristics of highly under-expanded jets with several different nozzle geometries (circular, elliptical, square, and rectangular). The results showed significant differences in the formation and development of intercepted surges, with the elliptical jet having the slowest penetration rate. Yang et al. [27] used the RANS method, LES method, and the RANS-LES hybrid method to simulate the fluid field of submerged cavitation water jets and analyzed the accuracy of different turbulence models in predicting jet cavitation. The results showed significant deviations in RANS, while RANS-LES and LES models showed higher precision.

Recent research has begun integrating fluid dynamics with multi-objective parameter optimization [28]. Li et al. [29] used genetic algorithms to optimize curved nozzle structural parameters for maximum output power. Uebel et al. [30] utilized quenching conversion concepts based on CFD to optimize and improve system performance and obtained feasible design parameters for a quenching reactor. Qian et al. [31] conducted experiments to obtain the relationship between injection distance and nozzle diameter, establishing a mathematical model to identify optimal injection distances for each nozzle diameter. Edeling et al. [32] used a Bayesian algorithm, calibrated with the Launder–Sharma  $k$ -model, to predict new boundary layer flows and analyze errors.

Response surface methods are frequently employed to explore the nonlinear effects of numerous variables on the response variable in a particular range and alter them based on practical demands [33]. Han et al. [34] used the response surface methodology to optimize the internal structural parameters for the key part of a straight cone nozzle, with the flow coefficient used as the objective function. Zhang et al. [35] proposed a dual serpentine nozzle structure and analyzed the influence of key structural parameters on its aerodynamic

performance using computational fluid dynamics and the response surface methodology. They established an axial thrust coefficient response model to understand interactions between exit aspect ratio, export area ratio, and nozzle outlet width ratio. Wang et al. [36] established a response surface method model with experimental impact force characteristics as dependent variables and nozzle structure parameters as separate variables. This model was used to calculate the optimal parameter solution. Using results from impact force and cleaning performance experiments, it was verified that the experimental errors were all less than 5%, indicating high reliability.

This paper establishes a response surface fitting model between the structural parameters of the cavitation nozzle and the peak gas-phase volume fraction inside the nozzle. The model, developed using Large Eddy Simulation and the response surface method, identifies optimal structural parameters. The optimized nozzle is then analyzed experimentally.

## 2. Numerical Simulation Model and Physical Model

### 2.1. Governing Equations of Large Eddy Simulation

Large Eddy Simulation decomposes turbulence into large-scale and small-scale vortices using a filter function. The large-scale vortices are directly solved using the N-S equation, while small-scale vortices are processed by the sublattice sub-scale model. In this study, the water jet cavitation phenomena, caused by the nozzle structure, results in a gas–liquid two-phase fluid. This fluid is considered incompressible and can be calculated by filtering the three-dimensional incompressible governing equations [37]:

$$\frac{\partial \bar{u}_i}{\partial x_i} = 0 \tag{1}$$

$$\frac{\partial \bar{u}_i}{\partial t} + \frac{\partial \bar{u}_i \bar{u}_j}{\partial x_j} = -\frac{1}{\rho} \frac{\partial \bar{p}}{\partial x_i} + \nu \frac{\partial^2 \bar{u}_i}{\partial x_i \partial x_j} - \frac{\partial \tau_{ij}}{\partial x_j} \tag{2}$$

$$\tau_{ij} - \frac{\delta_{ij}}{3} \tau_{kk} = -2\nu_\tau S_{ij} \tag{3}$$

where  $\bar{u}_i$  and  $\bar{u}_j$  are the instantaneous velocities of the fluid;  $x_i$  denotes the 3D coordinate direction;  $\rho$  and  $p$  represent the fluid density and fluid pressure, respectively;  $\tau_{ij}$  is the sub-grid scale stress between the large- and small-scale vortices;  $\delta_{ij}$  is Kronecker’s delta;  $\nu_\tau$  is the eddy viscosity; and  $S_{ij}$  is the resolved scale strain rate tensor.

The vortex viscosity coefficients are derived using the WALE model based on the velocity gradient’s invariance. The governing equations of the WALE model are as follows [38]:

$$\mu_t = \rho L_s^2 \frac{(S_{ij}^d S_{ij}^d)^{\frac{3}{2}}}{(\bar{S}_{ij} \bar{S}_{ij})^{\frac{5}{2}} + (S_{ij}^d S_{ij}^d)^{\frac{5}{4}}} \tag{4}$$

$$L_s = \min(kd, C_w V^{\frac{1}{3}}) \tag{5}$$

$$S_{ij}^d = \frac{1}{2} (\bar{g}_{ij}^2 + \bar{g}_{ji}^2) - \frac{1}{3} \delta_{ij} \bar{g}_{kk}^2, \bar{g}_{ij} = \frac{\partial \bar{u}_i}{\partial x_j} \tag{6}$$

where  $L_s$  is the length of the sub-grid scale;  $C_w$  is the WALE model constant, taken as 0.35 in the current work;  $d$  represents the distance to the proximate wall;  $k$  represents the von Karman constant; and  $V$  is the computational cell volume.

### 2.2. Computational Grid and Boundary Conditions

In this study, an organ pipe was connected behind a Helmholtz nozzle to form a dual-chamber composite nozzle. When the fluid flows into the Helmholtz chamber at high speed from the inlet, due to the sudden increase in cross-section, the high-speed fluid will form a submerged free jet after entering the Helmholtz chamber. The original low-speed fluid in the chamber comes into contact with it and forms a shear layer at the outer boundary of

the jet on the contact surface. The fluid within the boundary zone of a free jet undergoes entrainment with the nearby stationary fluid, causing the free jet to be in a reverse pressure state. At the same time, a shedding vortex is formed, which propagates downstream and interacts with the colliding wall to generate backflow, resulting in oscillation. When the jet enters the accordion tube and passes through the contracted section, it can generate pressure excitation in the fluid and feed back the pressure excitation to the resonant cavity, forming feedback pressure oscillation. According to transient flow theory, if the frequency of pressure excitation matches the natural frequency of the nozzle resonant cavity, the organ tube chamber will amplify the incoming flow from the Helmholtz chamber, which can transform the shear layer vortex of the jet into a large structure of separated annular vortex. The intermittent vortex circulation of this large structure can enhance cavitation, that is, generate cavitation jet at the outlet, thereby improving its erosion and cleaning ability. Figure 1 shows a geometric model of the Helmholtz–organ pipe composite nozzle, and the parameters are provided in Table 1.

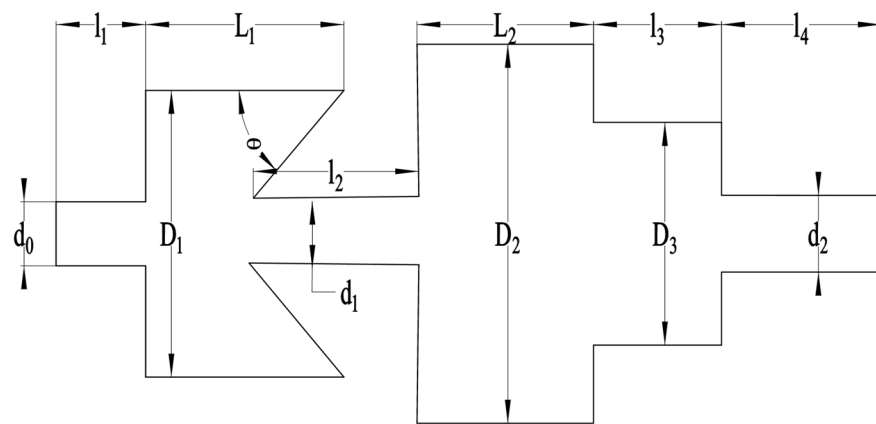


**Figure 1.** Composite nozzle model geometry.

**Table 1.** Composite nozzle structural parameters.

Position	Symbol/Unit	Dimensional Parameter
Inlet diameter	$d_0/\text{mm}$	6
Length of inlet straight section	$l_1/\text{mm}$	5
Helmholtz chamber diameter	$D_1/\text{mm}$	12–16
Helmholtz chamber length	$L_1/\text{mm}$	7–11
Helmholtz chamber angle	$\theta/^\circ$	60
Connection runner diameter	$d_1/\text{mm}$	2–8
Connection runner length	$l_2/\text{mm}$	6
Organ pipe resonant cavity diameter	$D_2/\text{mm}$	10
Diameter of the middle chamber of the organ pipe	$D_3/\text{mm}$	6
Organ pipe resonant cavity length	$L_2/\text{mm}$	6
Length of the cylindrical section of organ pipe	$l_3/\text{mm}$	4
Length of diffusion section	$l_4/\text{mm}$	5
Outlet diameter	$d_2/\text{mm}$	2

The computational domain for the submerged flow field is a cylinder having the diameter of 30 mm with the length of 100 mm, where it must be ensured that the fluid field develops properly in the composite nozzle. In this study, CFD grid generation was carried out using Fluent Meshing in ANSYS 2021R1 software. Polyhedral grids were used for meshing the geometry, and a denser grid was created in the composite nozzle jet's core region, as well as shear layers near the exit. To verify grid independence, the model was simulated for four sets of grids with different grid sizes. The results of the peak gas-phase volume fraction, as shown in Figure 2, indicate that as the amount of grid cells grew from

1,861,356 to 2,792,034 altogether, the change of the peak gas-phase volume fraction was less than 2.9%. Hence, the grid with 1,861,356 cells was used in the later models. The overall mesh quality of the selected grid was about 0.7, which meets the computational requirement of Large Eddy Simulations.

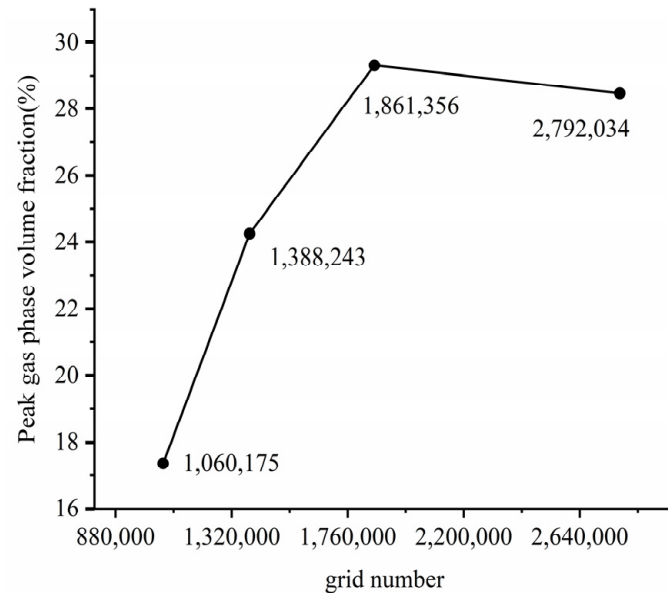


**Figure 2.** Effect of grid quantity on peak gas-phase volume fraction.

The final mesh of computational domain and boundary settings are shown in Figure 3. The pressure inlet was set at 10 MPa, while the output was set to 0 MPa. The ambient pressure was set at 101,325 Pa, with a turbulence intensity of 5% and a turbulent viscosity ratio of 10; additionally, a non-sliding wall surface was used. The fluid medium was pure water with a saturation vapor pressure of 3540 Pa. The WALE model was selected for LES as a sub-grid model, and the pressure–velocity coupled momentum equation was calculated using the PISO algorithm. Because cavitation is a complex unstable process, transient simulation was used in this research. The grid number of 1,861,356 was taken as the model, and the time step was  $1 \times 10^{-4}$  s,  $1 \times 10^{-5}$  s,  $1 \times 10^{-6}$  s, and the time independence test was conducted for the selected grid number. The calculated results are shown in Table 2. The simulation results changed greatly when the time step size changed from  $1 \times 10^{-4}$  s to  $1 \times 10^{-5}$  s, but when the time step is further reduced, the change in the results is relatively small. It can be concluded that when the transient time step is less than  $1 \times 10^{-5}$  s, the results of CFD simulation are independent of the time step, resulting in the time step of  $1 \times 10^{-5}$  s and the iteration step of 1000. The computational residuals for each time step of each conservation equation are less than  $1 \times 10^{-6}$ .

**Table 2.** Results of the time step size independence tests.

Time step size (s)	$1 \times 10^{-4}$	$1 \times 10^{-5}$	$1 \times 10^{-6}$
Peak gas-phase volume fraction (%)	29.06	29.32	29.33

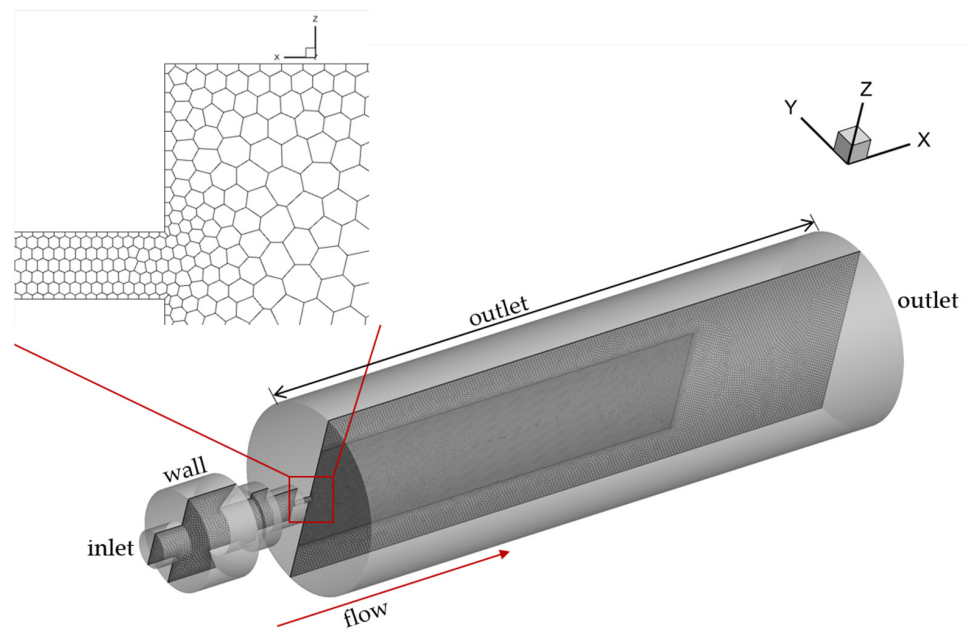


Figure 3. Mesh of computational domain and boundary settings.

### 3. Response Surface Method Design

The response surface technique aims to find the optimal solution by specifying a range of values for each variable. It involves conducting a finite number of tests and building a polynomial fit to approximate the relationship function between each factor [39,40]. The formula for the response surface method is as follows [41]:

$$y = \beta_0 + \sum_{i=1}^n \beta_i x_i + \sum_{i=1}^n \beta_{ii} x_i^2 + \sum_{i < j}^n \beta_{ij} x_i x_j + \varepsilon \tag{7}$$

The above equation includes the constant, linear, squared, and interaction terms, along with an error term. In Equation (7),  $n$  is the number of independent variables;  $\varepsilon$  is the total error;  $\beta_0$ ,  $\beta_i$ ,  $\beta_{ii}$ , and  $\beta_{ij}$  are the regression coefficients; and  $x$  is the investigation factor.

This study adopted the Box–Behnken Design (BBD) suitable for 2–5 factors in response to surface methodology. The experiments considered the peak gas-phase volume fraction as the dependent variable because the volume fraction of the gas phase can effectively reflect the effectiveness of cavitation; it can also reflect the cleaning ability of the composite nozzle, while the independent variables were taken as the diameter ( $D_1$ ), length ( $L_1$ ), and connecting channel diameter ( $d_1$ ) of the Helmholtz chamber in the composite nozzle. The design included three factors, A, B, and C, at three levels:  $-1$ ,  $0$ , and  $1$ . The coding and actual values for each design factor in the composite nozzle are displayed in Table 3.

Table 3. Levels of independent variables.

Variable	Coded Variables	Variable Levels		
		$-1$	$0$	$1$
$L_1$ /(mm)	A	7	9	11
$D_1$ /(mm)	B	12	14	16
$d_1$ /(mm)	C	2	5	8

According to Table 3, the experimental plan was designed with 17 sets of test points. The initial 12 sets were used for factor analysis, and the remaining 5 sets were used to estimate the experimental error. The final experimental plan and response values by simulation are shown in Table 4.

**Table 4.** Experimental design and results.

Run	Variables			Peak Gas-Phase Volume Fraction $V$ (%)
	A: $L_1$ /(mm)	B: $D_1$ /(mm)	C: $d_1$ /(mm)	
1	7	12	5	16.1516
2	11	12	5	26.2346
3	7	16	5	26.4647
4	11	16	5	20.3565
5	7	14	8	18.75
6	11	14	8	13.2654
7	7	14	2	24.364
8	11	14	2	30.5335
9	9	12	8	12.415
10	9	16	8	17.369
11	9	12	2	24.2589
12	9	16	2	25.1698
13	9	14	5	29.123
14	9	14	5	29.328
15	9	14	5	32.1356
16	9	14	5	28.7596
17	9	14	5	30.2115

## 4. Results and Discussion

### 4.1. Response Surface Analysis

Regression fitting was performed using the data from Table 4, involving multiple interactions to establish a predictive regression equation. This equation relates the peak gas-phase volume fraction of the composite nozzle to several factors:

$$V = 29.91 + 0.5825A + 1.29B - 5.32C - 4.05AB + 2.91AC + 1.01BC - 2.84A^2 - 4.77B^2 - 5.34C^2 \quad (8)$$

ANOVA was used to analyze the regression equation, and the results are presented in Table 5. Analysis reveals that the primary term  $C$ , and the secondary terms  $B^2$  and  $C^2$  have significant effects on the peak gas-phase volume fraction ( $p \leq 0.01$ ). The primary term  $B$ , interaction terms  $AB$  and  $AC$ , and secondary term  $A^2$  also significantly affect it ( $p \leq 0.05$ ). Other terms were found to have no significant effect. The  $F$  values in Table 5 indicate the degree of influence of three factors on the peak gas-phase volume fraction, as follows: connection channel diameter ( $C$ ) > Helmholtz chamber diameter ( $B$ ) > Helmholtz chamber length ( $A$ ). The  $p$ -value of this overall model ( $p < 0.001$ ) reached a high significance level, and the error of the out-of-fit term ( $p = 0.6848 > 0.05$ ) was found to be not significant. This indicates that the model is quite accurate and stable. The regression coefficient  $R^2$  of the model is 0.9838. This indicates that 98.38% of the variability in the data are accounted for by the model, suggesting a strong fit for substituting the experimental results. The adjusted  $R^2$  was 0.9630, which suggests that the model can explain 96.30% of the variance in the peak gas-phase volume fraction after adjusting for the number of predictors in the model. The difference between adjusted  $R^2$  and the predicted  $R^2$  is lower than 0.2. This indicates that the predicted values of the model are very close to experimental values, further indicating its high reliability.

Figure 4 shows the normal probability distribution of residuals and the distribution of residuals and predicted values, respectively. From Figure 4a, it can be seen that the normal probability distribution of residuals approximates a straight line, indicating reliable fitting results for the model's independent variables and response values. Figure 4b displays the externally studentized residuals of the model predictions against the predicted values of the model. The figure shows that the residuals are distributed randomly and irregularly. Based on the above judgment conditions, it can be concluded that the peak gas-phase

volume fraction model of the composite nozzle, obtained via the response surface method, exhibits good adaptability and conforms to the inspection principles.

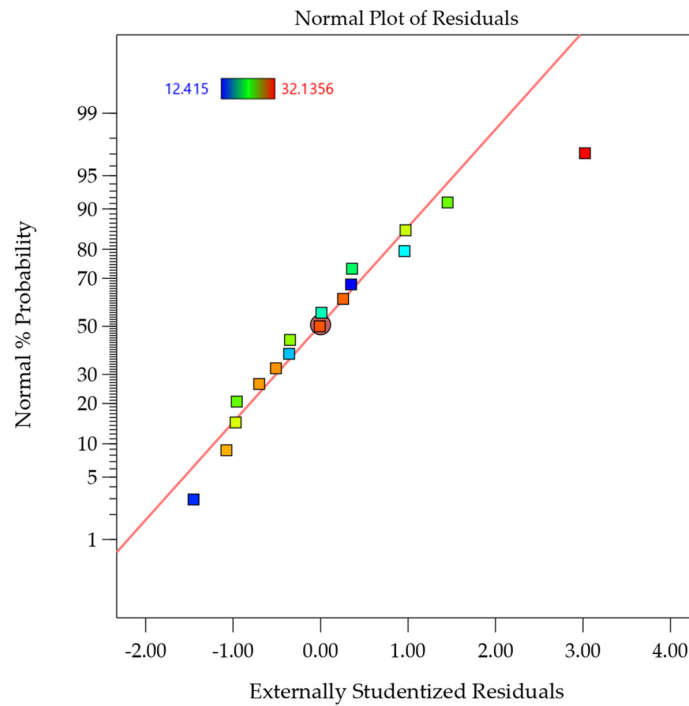
**Table 5.** ANOVA results of regression model.

Source	Sum of Squares	df	Mean Square	F Value	<i>p</i> Value	
Model	622.42	9	69.16	47.26	<0.0001	Significant
A	2.71	1	2.71	1.85	0.2155	
B	13.26	1	13.26	9.06	0.0197	
C	226.07	1	226.07	154.47	<0.0001	
AB	65.54	1	65.54	44.78	0.0003	
AC	33.95	1	33.95	23.20	0.0019	
BC	4.09	1	4.09	2.79	0.1386	
A <sup>2</sup>	34.02	1	34.02	23.24	0.0019	
B <sup>2</sup>	95.70	1	95.70	65.39	<0.0001	
C <sup>2</sup>	120.11	1	120.11	82.07	<0.0001	
Residual	10.24	7	1.46			
Lack of fit	2.92	3	0.9729	0.5312	0.6848	Not significant
Pure Error	7.33	4	1.83			
Cor Toal	632.66	16				
R <sup>2</sup>					0.9838	
Adjusted R <sup>2</sup>					0.9630	
Predicted R <sup>2</sup>					0.9081	

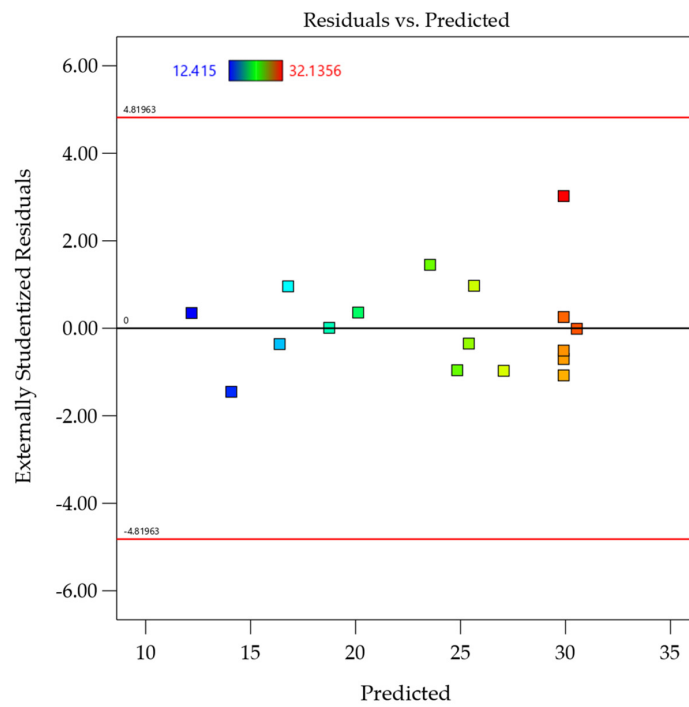
Figures 5–7 show the surface response plots for the peak gas-phase volume fraction of the composite nozzle at different values of *A*, *B*, and *C*, with one variable set at a level of 0. A larger slope indicates greater factor influence. It can be seen from Figure 5 that with a fixed diameter of the connecting runner  $d_1$ , the peak gas-phase volume fraction has a tendency to first increase and then decrease with the increase in the diameter of the Helmholtz chamber, peaking at a chamber diameter of 13.6 mm. When the diameter of the Helmholtz chamber is less than 13 mm, due to limited chamber space, cavitation bubbles become blocked in the chamber, energy is disrupted, and the vortex ring cannot effectively feedback upstream, resulting in a small gas-phase volume. Until the diameter of the Helmholtz chamber reaches 13.6 mm, the degree of cavitation significantly increases, and the gas-phase volume fraction reaches its peak. However, when the diameter exceeds 13.6 mm, the chamber space and feedback distance of the bubbles increase, and more bubbles stay near the collision wall, causing energy dissipation and reducing cavitation performance. Figure 6 shows a similar increase and decrease effect of the connecting runner diameter  $d_1$  on the peak gas-phase volume fraction. As the length of the Helmholtz chamber increases, the peak gas-phase volume fraction also increases. Due to the increase in length, there is enough space inside the chamber to develop and grow, forming large-scale vortex rings. However, when the length is large, it can also lead to a reduction in cavitation. The slope of the response surface in Figure 7 is greater than that in Figures 5 and 6, showing that modifications in *B* and *C* have a considerable effect on the peak gas-phase volume percent. Because the connection runner diameter is less than 2.9 mm, the energy inside the chamber is disrupted, which is not conducive to cavitation. When the connection runner diameter increases from 2 mm to 2.9 mm, the gas-phase volume fraction also increases.

After conducting response surface analysis and solving the fitted predictive regression equation, the value range of the three factors was set. The objective function was set to the greatest value of the peak gas-phase volume fraction, leading to the determination of the optimal size of the composite nozzle, as shown in Table 6. The predicted peak gas-phase volume fraction under these conditions was 31.747%. In order to validate the accuracy of this fitting model, numerical simulations of the optimized structure were carried out, resulting in an actual peak gas-phase volume fraction of 32.41%. The peak gas-phase volume fraction of the optimized nozzle was significantly improved; compared

to the same type of Helmholtz single-chamber nozzle [14], the gas-phase volume fraction increased by 189% and the relative error between the predicted and simulated values obtained by the response surface method under the same operating conditions was 2.04%. This small error confirms the reliability and accuracy of the model obtained by the response surface method.



(a)



(b)

**Figure 4.** Residual plots. (a) Normal probability distribution of residual; (b) residuals vs. predicted values.

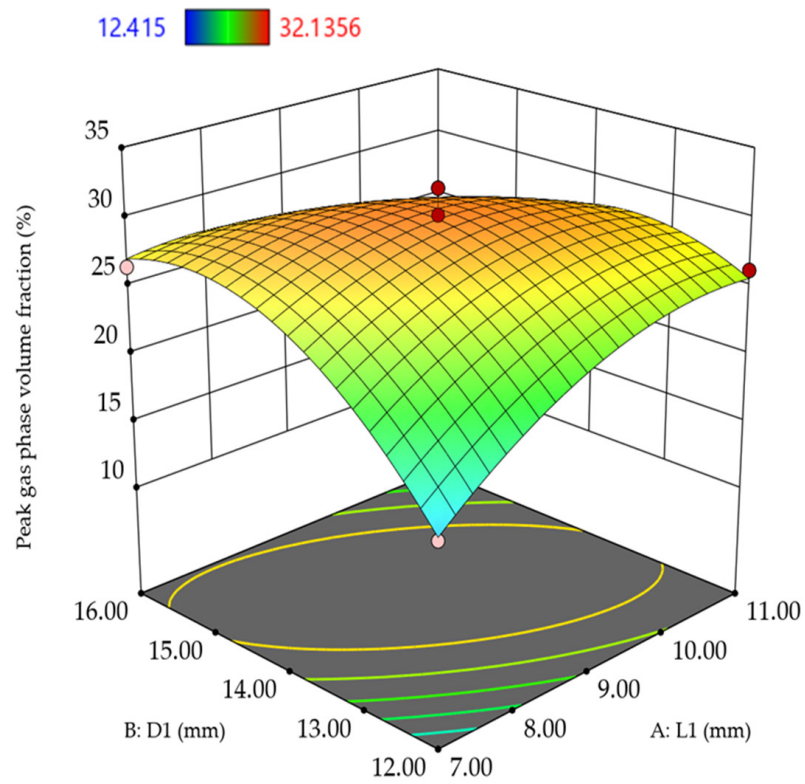


Figure 5. Peak gas-phase volume fraction of  $D_1-L_1$  response surface.

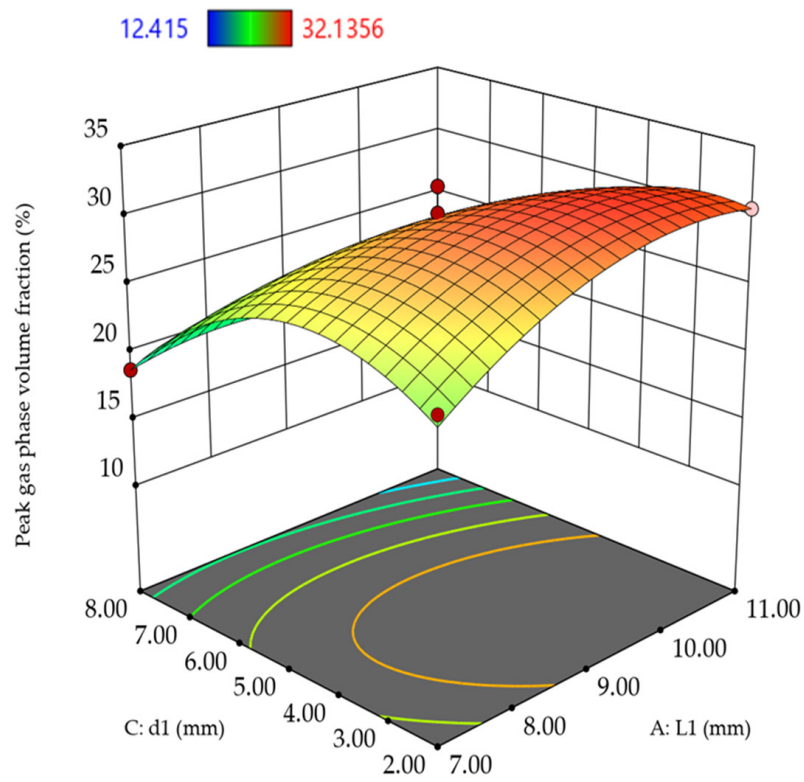
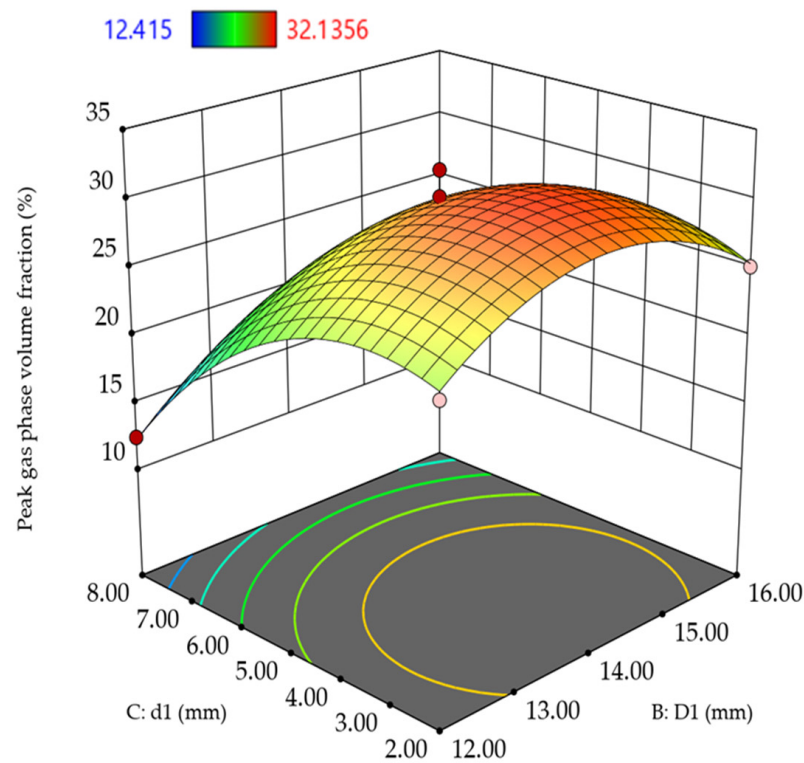


Figure 6. Peak gas-phase volume fraction of  $d_1-L_1$  response surface.



**Figure 7.** Peak gas-phase volume fraction of  $d_1$ – $D_1$  response surface.

**Table 6.** Parameters after nozzle optimization.

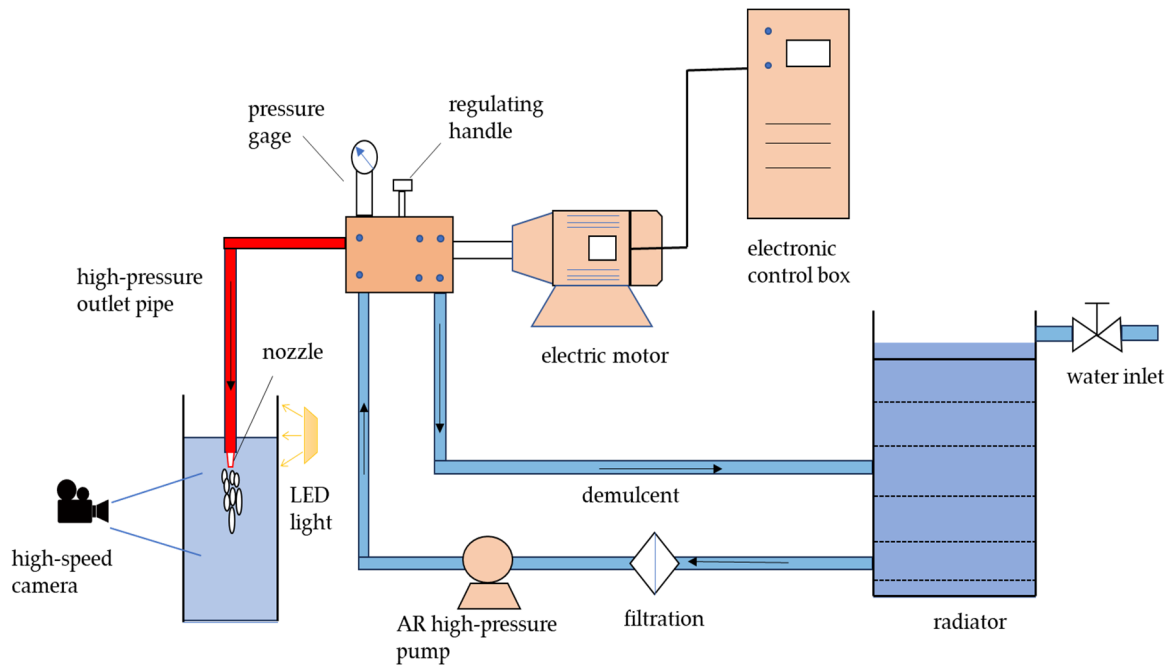
Structure	$d_1$ (mm)	$D_1$ (mm)	$L_1$ (mm)
Size	2.9	13.6	10.1

#### 4.2. Experimental Analysis of Cavitation Cloud Characteristics

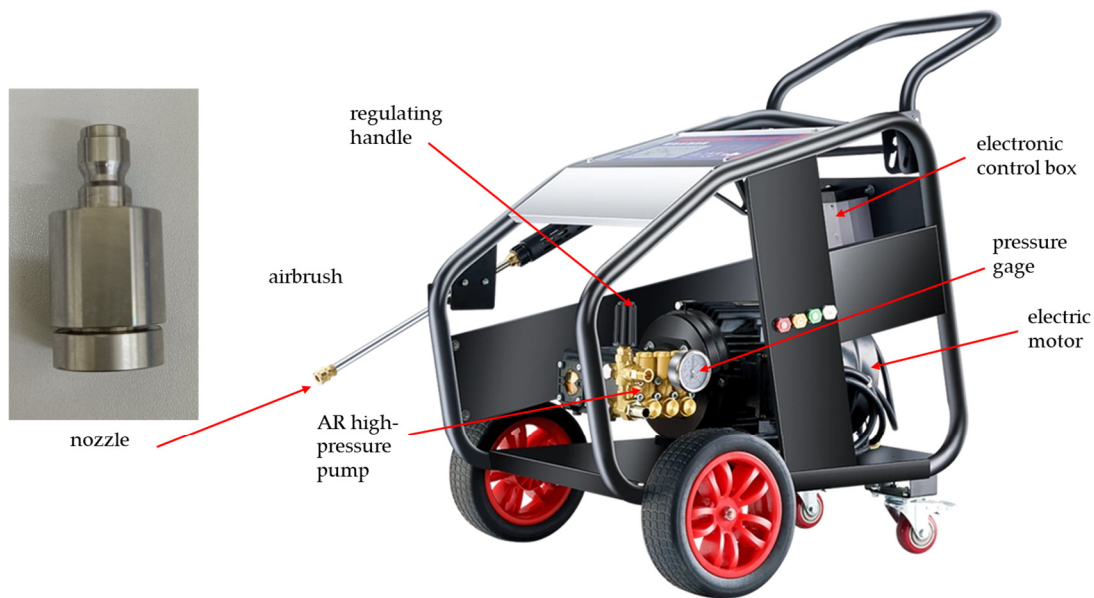
Figure 8a presents a schematic diagram of the cavitation jet experimental system. This system was mainly composed of a plunger pump, water tank, composite nozzle, motor, and high-speed camera. The experiment required high pressure, which was supplied by an AR high-pressure piston pump. It has a maximum operating pressure of 20 MPa. The experiments used clean water at 25 °C as the medium, with an inlet pressure of 10 MPa, and were conducted under submerged conditions. The composite nozzle adopted the optimized parameters—listed in Table 6—obtained using the response surface method. The nozzle along with the test setup are shown in Figure 8b. A high-speed camera was used to record the development and evolution of cavitation clouds at the submerged nozzle, while a pressure sensor was used to record the impact force. The experimental photos are shown in Figure 9.

Visualization experiments were conducted on the composite nozzle using the aforementioned experimental equipment. The cavitation clouds, as captured in Figure 9, are organized according to their development over time, as shown in Figure 10a. This process can be divided into three stages: the nascent stage (0–100  $\mu$ s), the developmental stage (100–1500  $\mu$ s), and the abscission and collapse stage (1500–1900  $\mu$ s). In the nascent stage of cavitation, the fluid is ejected from the nozzle into a stationary flow field. The interaction between the jet and the stationary fluid generates a pressure difference and shear flow, promoting the generation and development of bubbles. The minimum cavitation range is concentrated at the nozzle outlet. In the developmental stage, as fluid continues to eject from the jet, the length of the cavitation cloud increases gradually. Under the influence of jet shear, the high-speed flow diffuses to the surrounding area, leading to symmetric bubble distribution. The cavitation volume ratio in the red area increases to 0.7. With the

continued impact of subsequent jets on the tail of the cavitation bubbles, the tails begin to collapse inward. In the abscission and collapse stage, the cavitation cloud, at its maximum of around 100 mm, begins to detach from the jet, as shown by the red dashed line in Figure 10a. The maximum cavitation volume fraction decreases, and the cavitation begins to collapse. Figure 10b shows the simulation results using the Large Eddy Simulation with the WALE model.



(a)



(b)

**Figure 8.** Test platform for the high-pressure submerged jet. (a) Schematic diagram. (b) Photo of the experimental platform.



Figure 9. The experimental photos.

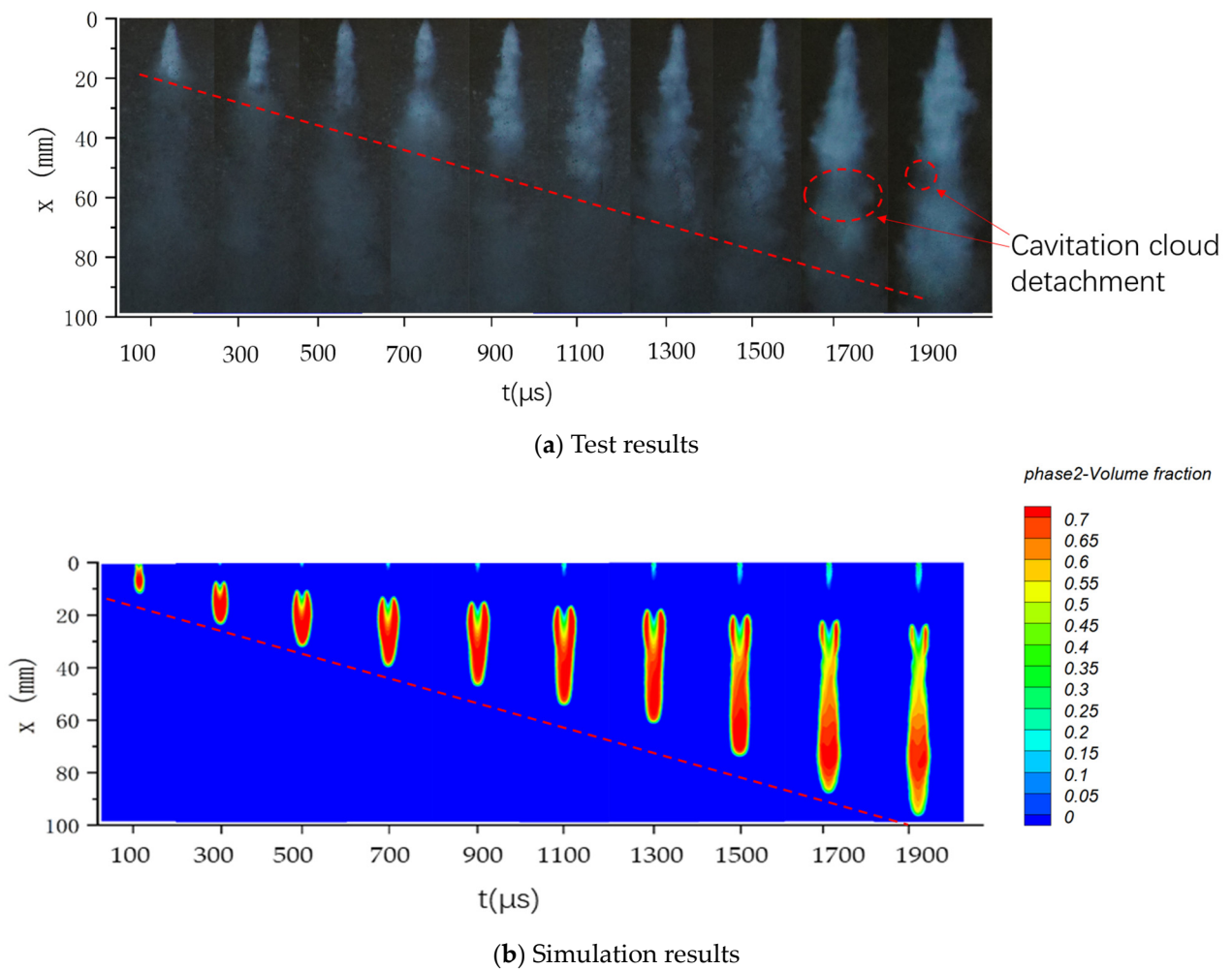
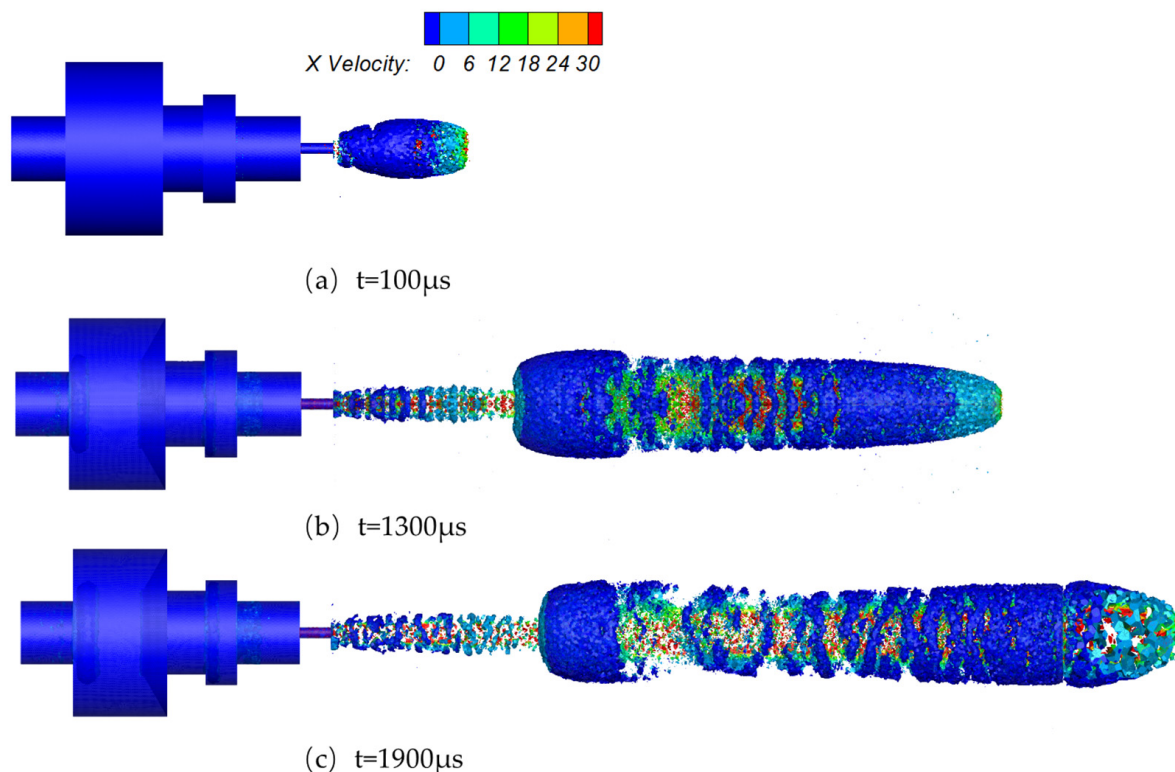


Figure 10. The evolution process of cavitation clouds of composite nozzles. (a) Test results. (b) Simulation results.

By comparing the numerical simulation with the experimental images, as can be seen from the red sloping dotted line, it is found that the evolution process of cavitation clouds is roughly the same. However, differences in grid numbers and numerical simulation models prevent the experimental images from aligning perfectly with the simulations.

The normalized Q-criterion, where the value of Q denotes the level of vortex strength, was used to form simulations in order to identify and display the vortex's features. The vortex structure's temporal evolution is depicted in Figure 11. At  $Q = 30,000$ , the emphasis is on the creation of coherent structures inside the jet, which contains several scale vortices. At  $t = 100 \mu\text{s}$ , in the nascent stage, high flow velocity at the nozzle outlet results in dense, small-scale vortices. At  $t = 1300 \mu\text{s}$ , during the period of cavitation development, small-scale vortices near the nozzle increase, and the conical large-scale vortex at the rear end elongates and fractures. At  $t = 1900 \mu\text{s}$ , in the abscission and collapse stage of cavitation, the collapse of cavitation bubbles generates energy that causes disturbance to the fluid, breaking down the vortices into smaller scales and leading to an increase in the overall length of vortices. As illustrated in Figure 11, the flow velocity decreases outward from the central axis throughout the entire process, with small-scale vortices distributed along the axis and large-scale vortices present on the outer side. The Helmholtz structure causes the uniform inlet flow to oscillate, forming a "Ring Vortices" structure at the nozzle outlet.



**Figure 11.** Vortex structure evolution over time.

Figure 12 shows the curve of impact force variation over time in tests and simulations with an inlet pressure of 10 MPa and a target distance of 20 mm. Here,  $F$  is the impact force on the target surface, and  $t$  is the test time. Between 0.05 and 0.25 S, the simulated impact force oscillates between 256 and 297 N, with a pulsation amplitude of 41 N. The impact force measured in the test oscillates between 260 and 289 N, with a pulsation amplitude of 29 N. The error between the test and simulation is in the range of 1.5% to 2.7%, which verifies the reliability of the optimized nozzle. The higher simulated values compared to test results are attributed to the measurement losses of transducer surface forces during testing.

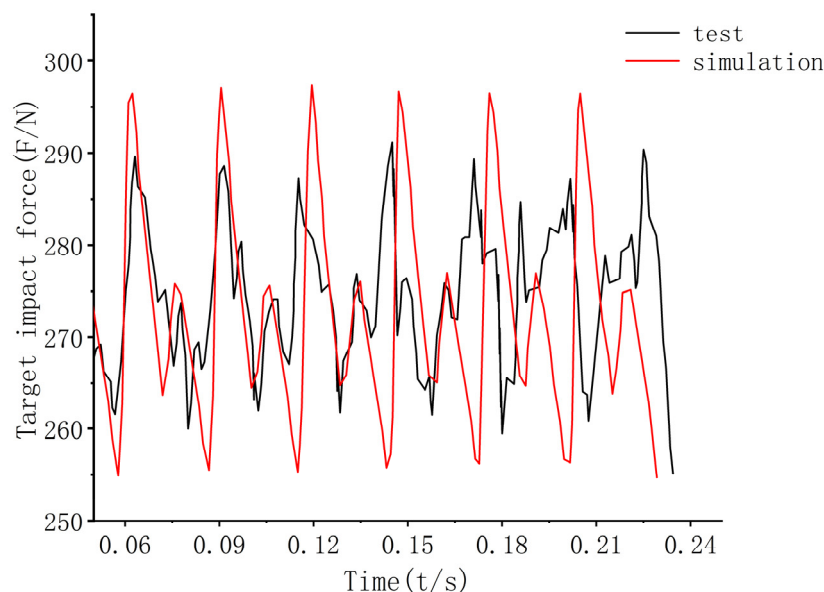


**Figure 12.** Comparison of target impact force between test and simulation results.

## 5. Conclusions

This paper optimized the composite nozzle, which is composed of a Helmholtz–organ pipe. It combined CFD Large Eddy Simulation with the response surface method. A high-pressure water jet cavitation visualization experiment system has been established, and a comparative study of the cavitation cloud evolution has been carried out using a high-speed camera. Through design optimization and experimentation, the following conclusions were reached:

- (1) The BBD response surface methodology was used to construct a predictive regression equation between the composite nozzle parameters and the peak gas-phase volume fraction. A total of 98.38% of the data in the regression equation fitted well with the actual simulation results, reaching a highly significant level. This can replace numerical calculations to predict the results.
- (2) Among the single factors, the diameter of the connecting channel and the diameter of the Helmholtz chamber significantly influenced the peak gas-phase volume fraction. Taking the peak gas-phase volume fraction as the response value, the influence of three factors, namely the diameter of the Helmholtz chamber, the length of the Helmholtz chamber, and the diameter of the connecting flow channel, on the response value can be sorted as follows: connection channel diameter > Helmholtz chamber diameter > Helmholtz chamber length.
- (3) The optimized structural parameters of the composite nozzle at an inlet pressure of 10 MPa were determined using the response surface method: the diameter of the connecting runner is 2.98 mm, the diameter of the Helmholtz chamber is 13.6 mm, and the length of the Helmholtz chamber is 10.1 mm. The peak gas-phase volume fraction achieved using the optimized parameters was 32.41%, with a relative error of 2.04% from the model prediction. The optimized composite nozzle showed a significant improvement in cavitation performance.
- (4) Visual experiments on the flow field of composite nozzles indicate that the simulation of the cavitation period matches the experimental photos, consistent with existing research. The nozzle-generated vortex is mainly distributed along the axis, with small-scale vortices at the nozzle outlet and a conical large-scale vortex at the far end of the nozzle outlet. Over time, large-scale vortices collapse into small-scale vortices. In the impact force testing experiment, the calculation results of the optimized composite nozzle scheme aligned well with the experimental model test results, verifying the optimization results and simulation accuracy.

Further experimental and numerical study is needed, such as observing the properties of cavitation clouds using particle image velocimetry (PIV) and using artificial neural network methods to solve the nonlinear multiparameter coupling problem of nozzles, establishing the relationship between the structure of cavitation jet nozzles and cavitation effects.

**Author Contributions:** Conceptualization, G.H. and C.Q.; Data curation, G.H., K.H. and J.G.; Investigation, W.Q., Y.Z., J.H. and H.H.; Methodology, G.H., M.S. and K.C.; Project administration, G.H. and C.Q.; Validation, W.Q. and M.S.; Writing—review and editing, G.H. and M.S. All authors have read and agreed to the published version of the manuscript.

**Funding:** This research was funded by the CSSC Guangxi Shipbuilding and Offshore Engineering Technology Collaboration Project: ZCGXJSB20226300222-06; Project of Qinzhou Science and Technology Source: 202116622; High-end Foreign Expert Introduction Plan: G2022033007L.

**Data Availability Statement:** The data presented in this study are available on request from the corresponding author.

**Acknowledgments:** We appreciate the anonymous reviewers' ideas to improve the manuscript. We appreciate the editors' work on the manuscript.

**Conflicts of Interest:** The authors declare no conflict of interest.

## Nomenclature

$\bar{u}_i, \bar{u}_j$	Instantaneous velocities of the fluid
$x_i$	3D coordinate direction
$\rho$	Fluid density
$p$	Fluid pressure
$\tau_{ij}$	Sub-grid scale stress
$\delta_{ij}$	Kronecker's delta
$\nu_\tau$	Eddy viscosity
$S_{ij}$	Resolved scale strain rate tensor
$L_s$	Length of the sub-grid scale
$C_w$	WALE model constant
$d$	Distance to the proximate wall
$k$	von Karman constant
$V$	Computational cell volume
$n$	The number of independent variables
$\epsilon$	Total error
$\beta_0, \beta_i, \beta_{ii},$ and $\beta_{ij}$	Regression coefficients
$x$	Investigation factor
Df	Freedom
Q	Magnitude of vortex intensity

## References

1. Johnson, V.E.; Kohl, R.E.; Thiruvengadam, A.; Conn, A.F. Tunnelling, fracturing, drilling, and mining with high speed water jets utilizing cavitation damage. In Proceedings of the 1st International Symposium on Jet Cutting Technology, Coventry, UK, 5–7 April 1972.
2. Wen, J.W.; Chen, C.; Campos, U. Experimental research on the performances of water jet devices and proposing the parameters of borehole hydraulic mining for oil shale. *PLoS ONE* **2018**, *13*, 32. [[CrossRef](#)] [[PubMed](#)]
3. Soyama, H. Cavitating Jet: A Review. *Appl. Sci.* **2020**, *10*, 7280. [[CrossRef](#)]
4. Soyama, H. Cavitation Peening: A Review. *Metals* **2020**, *10*, 270. [[CrossRef](#)]
5. Szolcek, M.; Cassineri, S.; Cioncolini, A.; Scenini, F.; Curioni, M. CRUD removal via hydrodynamic cavitation in micro-orifices. *Nucl. Eng. Des.* **2019**, *343*, 210–217. [[CrossRef](#)]
6. Shi Khan, N.S.; Hussanan, A.; Kumam, W.; Kumam, P.; Suttiarporn, P. Accessing the thermodynamics of Walter-B fluid with magnetic dipole effect past a curved stretching surface. *Zamm J. Appl. Math.* **2023**, *103*, e202100112. [[CrossRef](#)]
7. Luo, Y.; Zang, J.; Zheng, H. Flow Field and Gas Field Distribution of Non-Submerged Cavitation Water Jet Based on Dual-Nozzle with Concentric Configuration. *Water* **2023**, *15*, 2904. [[CrossRef](#)]
8. Jian-Jie, W.; Li-Yu, C.; Xia-Ming, Y.; Zhen-Ying, X.U.; Yun, W. Research Progress of the Cavitation Water-jet Application. *J. Netshape Form. Eng.* **2016**, *8*, 156–162.

9. Zhao, F.; Wang, X.; Xu, W.; Zhu, H. Study on Different Parameters of the Self-Excited Oscillation Nozzle for Cavitation Effect under Multiphase Mixed Transport Conditions. *J. Mar. Sci. Eng.* **2021**, *9*, 1159. [[CrossRef](#)]
10. Wan, C.H.; Wang, R.H.; Zhou, W.D.; Li, L.P. Experimental study on viscosity reduction of heavy oil by hydrogen donors using a cavitating jet. *RSC Adv.* **2019**, *9*, 2509–2515. [[CrossRef](#)]
11. Wang, Z.L.; Lei, Y.; Wu, Z.H.; Wu, J.; Zhang, M.L.; Liao, R.Q. Structure Size Optimization and Internal Flow Field Analysis of a New Jet Pump Based on the Taguchi Method and Numerical Simulation. *Processes* **2023**, *11*, 24. [[CrossRef](#)]
12. Cui, L.; Ma, F.; Cai, T. Investigation of Pressure Oscillation and Cavitation Characteristics for Submerged Self-Resonating Waterjet. *Appl. Sci.* **2021**, *11*, 6972. [[CrossRef](#)]
13. Haosheng, C.; Jiang, L.; Darong, C.; Jiadao, W. Damages on steel surface at the incubation stage of the vibration cavitation erosion in water. *Wear* **2008**, *266*, 69–75. [[CrossRef](#)]
14. Dong, J.; Meng, R.; Chen, J.; Liu, M.; Zhong, X.; Pan, X. Numerical Investigation on Cavitation Jet in Circular Arc Curve Chamber Self-Excited Oscillation Nozzle. *J. Mar. Sci. Eng.* **2023**, *11*, 1391. [[CrossRef](#)]
15. Yang, Y.; Li, W.; Shi, W.; Zhang, W.; El-Emam, M.A. Numerical Investigation of a High-Pressure Submerged Jet Using a Cavitation Model Considering Effects of Shear Stress. *Processes* **2019**, *7*, 541. [[CrossRef](#)]
16. Dong, W.; Yao, L.; Luo, W. Numerical Simulation of Flow Field of Submerged Angular Cavitation Nozzle. *Appl. Sci.* **2023**, *13*, 613. [[CrossRef](#)]
17. Wang, G.W.; Yang, Y.F.; Wang, C.; Shi, W.D.; Li, W.; Pan, B. Effect of Nozzle Outlet Shape on Cavitation Behavior of Submerged High-Pressure Jet. *Machines* **2022**, *10*, 17. [[CrossRef](#)]
18. Stanley, S.A.; Sarkar, S.; Mellado, J.P. A study of the flow-field evolution and mixing in a planar turbulent jet using direct numerical simulation. *J. Fluid Mech.* **2002**, *450*, 377–407. [[CrossRef](#)]
19. Im, K.S.; Cheong, S.K.; Powell, C.F.; Lai, M.C.D.; Wang, J. Unraveling the Geometry Dependence of In-Nozzle Cavitation in High-Pressure Injectors. *Sci. Rep.* **2013**, *3*, 2067. [[CrossRef](#)]
20. Li, L.D.; Xu, Y.; Ge, M.M.; Wang, Z.C.; Li, S.; Zhang, J.L. Numerical Investigation of Cavitating Jet Flow Field with Different Turbulence Models. *Mathematics* **2023**, *11*, 18. [[CrossRef](#)]
21. Liu, Z.M.; Li, Z.M.; Liu, J.B.; Wu, J.C.; Yu, Y.S.; Ding, J.W. Numerical Study on Primary Breakup of Disturbed Liquid Jet Sprays Using a VOF Model and LES Method. *Processes* **2022**, *10*, 20. [[CrossRef](#)]
22. Zhang, L.; Wang, Q.; Guan, W.; Cao, T.Y.; Duan, L.; Pachiannan, T.; He, Z.X. Large eddy simulations on asymmetrical atomization of the elliptical jet with cavitation. *Atom. Sprays* **2019**, *29*, 177–198. [[CrossRef](#)]
23. Khan, N.S.; Sriyab, S.; Kaewkhao, A.; Thawinan, E. Hall current effect in bioconvection Oldroyd-B nanofluid flow through a porous medium with Cattaneo-Christov heat and mass flux theory. *Sci. Rep.* **2022**, *12*, 19821. [[CrossRef](#)] [[PubMed](#)]
24. Kim, J.; Choi, H. Large eddy simulation of a circular jet: Effect of inflow conditions on the near field. *J. Fluid Mech.* **2009**, *620*, 383–411. [[CrossRef](#)]
25. Fang, Z.; Hou, W.; Xu, Z.; Guo, X.; Zhang, Z.; Shi, R.; Yao, Y.; Chen, Y. Large Eddy Simulation of Cavitation Jets from an Organ-Pipe Nozzle: The Influence of Cavitation on the Vortex Coherent Structure. *Processes* **2023**, *11*, 2460. [[CrossRef](#)]
26. Li, X.; Zhou, R.; Yao, W.; Fan, X. Flow characteristic of highly underexpanded jets from various nozzle geometries. *Appl. Therm. Eng.* **2017**, *125*, 240–253. [[CrossRef](#)]
27. Yang, Y.; Shi, W.; Tan, L.; Li, W.; Chen, S.; Pan, B. Numerical Research of the Submerged High-Pressure Cavitation Water Jet Based on the RANS-LES Hybrid Model. *Shock Vib.* **2021**, *2021*, 6616718. [[CrossRef](#)]
28. Wang, Z.; Sun, X.; Chen, S. Multi-objective parameters optimization design of self-excited oscillation pulsed atomizing nozzle. *J. Braz. Soc. Mech. Sci. Eng.* **2019**, *41*, 510. [[CrossRef](#)]
29. Li, W.H.; Liu, K.; Guo, Q.H.; Zhang, Z.M.; Ji, Q.L.; Wu, Z.J. Genetic Algorithm-Based Optimization of Curved-Tube Nozzle Parameters for Rotating Spinning. *Front. Bioeng. Biotechnol.* **2021**, *9*, 10. [[CrossRef](#)]
30. Uebel, K.; Rössger, P.; Prüfert, U.; Richter, A.; Meyer, B. CFD-based multi-objective optimization of a quench reactor design. *Fuel Process. Technol.* **2016**, *149*, 290–304. [[CrossRef](#)]
31. Qian, Y.L.; Bi, Y.X.; Zhang, Q.; Chen, H.Y. The optimized relationship between jet distance and nozzle diameter of a pulse-jet cartridge filter. *Powder Technol.* **2014**, *266*, 191–195. [[CrossRef](#)]
32. Edeling, W.N.; Cinnella, P.; Dwight, R.P.; Bijl, H. Bayesian estimates of parameter variability in the k- $\epsilon$  turbulence model. *J. Comput. Phys.* **2014**, *258*, 73–94. [[CrossRef](#)]
33. Wu, D.Z.; Wang, J.Y.; Miao, T.; Chen, K.Y.; Zhang, Z.L. Performance Optimization of FA-GGBS Geopolymer Based on Response Surface Methodology. *Polymers* **2023**, *15*, 1881. [[CrossRef](#)] [[PubMed](#)]
34. Yang, H.; Zhang, X.R.; Yuan, G.; Li, Z.L.; Zhang, F.B. Structure optimization of straight cone nozzle and its effect on jet impingement heat transfer. *Numer. Heat Tranf. A Appl.* **2023**, *13*. [[CrossRef](#)]
35. Zhang, X.Y.; Shan, Y.; Zhang, J.Z. Optimization and sensitivity analysis of double serpentine nozzles within confined layouts by response surface methodology. *Therm. Sci. Eng. Prog.* **2023**, *43*, 22. [[CrossRef](#)]
36. Wang, Y.; Wang, X.L.; Zhang, Z.L.; Li, Y.; Liu, H.L.; Zhang, X.; Hocevar, M. Optimization of a Self-Excited Pulsed Air-Water Jet Nozzle Based on the Response Surface Methodology. *Stroj. Vestn. J. Mech. Eng.* **2021**, *67*, 75–87. [[CrossRef](#)]
37. Piomelli, U. Large eddy simulations in 2030 and beyond. *Philos. Trans. R Soc. A* **2014**, *372*, 20130320. [[CrossRef](#)]
38. Ahmed, B.H.T.; Kanfoudi, H.; Zgolli, R.; Ennouri, M. Investigation of Subgrid-Scale Models in Large Eddy Simulation on the Unsteady Flow Around a Hydrofoil Using OpenFOAM. *Iran. J. Sci. Technol. Trans. Mech. Eng.* **2019**, *44*, 465–480.

39. Wang, J.; Wei, M.; He, J.; Wang, Y.; Ren, C. Optimization of Repair Process Parameters for Open-Arc Surfacing Welding of Grinding Rolls Based on the Response Surface Method. *Processes* **2022**, *10*, 321. [[CrossRef](#)]
40. Le, H.S.; Galal, A.M.; Alhamrouni, I.; Aly, A.A.; Abbas, M.; Saidi, A.S.; Truong, T.H.; Dahari, M.; Wae-hayee, M. Heat transfer efficiency optimization of a multi-nozzle micro-channel heat sink utilizing response surface methodology. *Case Stud. Therm. Eng.* **2022**, *37*, 18. [[CrossRef](#)]
41. Jiang, S.H.; Li, D.Q.; Zhou, C.B.; Zhang, L.M. Capabilities of stochastic response surface method and response surface method in reliability analysis. *Struct. Eng. Mech.* **2014**, *49*, 111–128. [[CrossRef](#)]

**Disclaimer/Publisher’s Note:** The statements, opinions and data contained in all publications are solely those of the individual author(s) and contributor(s) and not of MDPI and/or the editor(s). MDPI and/or the editor(s) disclaim responsibility for any injury to people or property resulting from any ideas, methods, instructions or products referred to in the content.